RSC Advances

PAPER

View Article Online
View Journal | View Issue

Cite this: *RSC Adv.*, 2025, **15**, 28870

Electrostatic self-assembly synthesized Fe-MOF/g-C_3N_4 S-scheme heterojunction for enhanced photocatalytic pollutant degradation

Hongqiang Xin, *[a] Jingpu Zhang,[b] Zeming Lin,[a] Wen Li[c] and Fei Ma *[b]

Received 10th July 2025
Accepted 10th August 2025

DOI: 10.1039/d5ra04928h

rsc.li/rsc-advances

Water-borne organic pollutants pose severe threats to human health, driving urgent demand for cost-effective, high-efficiency photocatalysts. In this work, a novel S-scheme heterojunction Fe-MOF/g-C_3N_4 photocatalyst is prepared through facile self-assembly. The porous composite exhibits a specific surface area of 97.414 $m^2\ g^{-1}$, providing abundant active sites. The optimized MCN3-10 composite (Fe-MOF : g-C_3N_4 = 3 : 10) demonstrates exceptional activity, achieving 99% rhodamine B (RhB) degradation under xenon lamp irradiation within 40 minutes. Its first-order rate constant (120.33 × 10^{-3} min^{-1}) represents 33.9-fold and 2.5-fold enhancements over pristine Fe-MOF and g-C_3N_4, respectively. The superior performance originates from the S-scheme heterojunction, which simultaneously enhances redox capabilities and facilitates efficient charge carrier separation, resulting in the production of abundant reactive species for pollutant degradation.

1 Introduction

The rapid evolution of industrialization has exerted an unprecedented impact on Earth's finite resources.[1] Freshwater, one of the most intensively utilized resources in both daily life and industry, is facing a critical challenge.[2] Water resources are increasingly contaminated by diverse pollutants originating from human activities, including heavy metals, organic compounds, and acidic or alkaline substances.[3–5] Notably, many organic pollutants possess complex, highly conjugated molecular structures, and it is difficult to naturally decompose, resulting in long-term environmental persistence.[6] Consequently, developing efficient and practical technologies for degrading these organic pollutants becomes urgent. Traditional methods for removing these contaminants, such as, membrane filtration, electrochemical treatment, ion exchange, chemical coagulation, adsorption, and biodegradation have been extensively studied.[7] However, they often entail high costs and generate secondary pollutants, limiting their large-scale application. In contrast, advanced oxidation processes (AOPs) are a promising and effective approach.[8] AOPs could generate highly reactive free radicals with strong oxidizing capacity, and could promote the breakdown of refractory organic matter into degradable substances and facilitate water purification.[9] Among AOPs, photocatalytic degradation of organic pollutants represents an innovative technology.[10] Specifically, the photocatalytic Fenton process utilizes the reaction between H_2O_2 and Fe^{2+} to generate highly oxidizing hydroxyl radicals (·OH).[11] It has attracted significant attentions due to its potential for efficient and environmentally friendly degradation of organic pollutants.

Iron-based metal–organic frameworks (Fe-MOFs) are prominent photocatalysts and heterogeneous catalysts for AOPs, primarily due to their abundant unsaturated coordination sites.[12–15] However, Fe-MOFs suffer from a limited visible-light response range and rapid recombination of photogenerated electron–hole pairs, which hinder their photocatalytic efficiency. To address these limitations, researchers have developed integrated heterostructures by coupling Fe-MOFs with semiconductors. For examples, He *et al.*[16] incorporated MIL-101(Fe) into TiO_2 to extend light absorption to the solar spectrum. Guo *et al.*[17] enhanced photocatalytic performance by combining carbon quantum dots (CQDs) with MIL-88B(Fe). In parallel, graphitic carbon nitride (g-C_3N_4) has also gained attentions as a novel non-metallic photocatalytic material,[18,19] but faces similar challenges, including charge recombination and material instability.[20,21] Recent studies show that combination of g-C_3N_4 with semiconductors (*e.g.*, TiO_2, Fe_3O_4, WO_3, In_2O_3) can mitigate these issues and enhance visible-light absorption.[22–25] For instance, Lu *et al.*[26] demonstrated that Pt/g-C_3N_4 composites exhibit a UV-Vis absorption red-shift, indicating expanded visible-light harvesting. Photoluminescence spectroscopy further confirmed that Pt loading could significantly suppresses electron–hole recombination. Huang *et al.* found that TiO_2/g-C_3N_4 composites could almost completely decompose RhB in aqueous solution under visible light within

[a]*Lanzhou Jiaotong University, New Energy and Power Engineering, 88 Anning West Road, Anning District, Lanzhou, Gansu, China. E-mail: klxhq@163.com*
[b]*Xi'an Jiaotong University, State Key Laboratory for Mechanical Behavior of Materials, 28 Xianning West Road, Xi'an, Shaanxi, China. E-mail: mafei@mail.xjtu.edu.cn*
[c]*Southwest Jiaotong University. Materials Science and Engineering, 999 Xi'an Road, Pidu District, Chengdu, Sichuan, China*

60 minutes.[27] Critically, iron-based MOFs (Fe-MOFs) provide distinctive structural and electronic properties over conventional semiconductors when hybridized with g-C_3N_4. Because Fe–O clusters in Fe-MOFs as visible-light sensitizers can complement the limited spectral range of g-C_3N_4 through interfacial energy transfer. Ultrahigh surface areas of Fe-MOFs impose confinement effects that disperse g-C_3N_4 layers, mitigating stacking-induced active site loss. Inherent Fe^{3+}/Fe^{2+} redox cycles enable self-Fenton activation of persulfates (PDS), that overcome the intrinsic limitations of both materials.[28–30] These advancements suggest that combining g-C_3N_4 with Fe-MOFs holds substantial promise for enhancing photocatalytic performance. Such hybrids could overcome the inherent limitations of both materials while synergistically leveraging their respective advantages.

In this study, Fe-MOF/g-C_3N_4 heterojunction was fabricated *via* a facile self-assembly method. The optimized structure of the Fe-MOF/g-C_3N_4 (named as MCN3-10) significantly enhanced its photocatalytic activity for RhB degradation, achieving 33.9-fold and 2.5-fold improvements over pristine Fe-MOF and g-C_3N_4 (CN), respectively. The results show that this remarkable performance enhancement is primarily attributed to the formation of an S-scheme heterojunction between Fe-MOF and g-C_3N_4. The heterojunction facilitates abundant reactive oxygen species (ROS) generation, enabling highly efficient RhB degradation.

2 Materials

2.1. Chemicals

Chemicals: iron(III) chloride hexahydrate ($FeCl_3 \cdot 6H_2O$) and Rhodamine B (RhB) were purchased from Tianjin Kemiou Chemical Reagent Co., Ltd. *N*,*N*-Dimethylformamide (DMF) was supplied by Dongying Fuyu Chemical Co., Ltd. Fumaric acid ($C_4H_4O_4$) was obtained from Damao Chemical Reagent Factory, and urea (CH_4N_2O) was sourced from Shanghai Macklin Biochemical Technology Co., Ltd. All chemicals were used as received without further purification.

2.2. Synthesis of g-C_3N_4 (CN), Fe-MOF and Fe-MOF/g-C_3N_4

2.2.1 Preparation of g-C_3N_4 (CN). A crucible containing 10 g of urea was covered with aluminium foil. Bulk C_3N_4 was synthesized by heating the urea to 550 °C at a heating rate of 5 °C min^{-1} in a muffle furnace, maintained for 4 hours, and then naturally cooled down to room temperature. The product was ground into powder, dispersed in 50 mL pure ethanol, and subjected to ultrasonic treatment for 18 hours. The suspension was then centrifuged, and the collected powder was dried to obtain g-C_3N_4.

2.2.2 Preparation of Fe-MOF. Fe-MOF was synthesized *via* a hydrothermal method. Specifically, 1.16 g fumaric acid and 1.62 g iron(III) chloride hexahydrate was dissolved in 100 mL of *N*,*N*-dimethylformamide (DMF) under continuous stirring. The mixture was heated at 120 °C for 2 hours. After cooling to room temperature, the product, MIL-88A (Fe-MOF), was collected and washed five times with deionized water *via* centrifugation to remove impurities.

2.2.3 Preparation of Fe-MOF/g-C_3N_4. Fe-MOF and g-C_3N_4 powders were thoroughly mixed and ground for 30 minutes. The resulting mixture was then calcined in a tube furnace at 350 °C for 2 hours to obtain porous Fe-MOF/CN heterojunction. The electrostatic self-assembly mechanism is detailed as follows: Fe-MOF, with unsaturated Fe^{3+} sites on its surface (exposing positive charges due to incomplete coordination), and g-C_3N_4, with terminal –NH and –OH groups (ionizing to generate surface negative charges under ambient conditions), undergo strong electrostatic attraction during grinding. This interaction drives intimate contact between the two components, forming a pre-heterojunction structure. Subsequent calcination at 350 °C (optimized to avoid structural collapse of either component) promotes the formation of covalent/coordinate bonds at the interface (*e.g.*, Fe–O–C or Fe–N–C linkages), consolidating the heterojunction while preserving the porous architecture. Based on the mass ratios of Fe-MOF to g-C_3N_4 (1 : 10, 2 : 10, 3 : 10, 4 : 10, and 5 : 10), the prepared samples were named as MCN1-10, MCN2-10, MCN3-10, MCN4-10, and MCN5-10, respectively.

2.3. Characterizations

The X-ray diffraction (XRD) patterns of the materials were obtained using Cu Kα radiation on a Bruker D8 Advance diffractometer. Fourier-transform infrared (FT-IR) spectra were recorded using an IN10 + IZ10 spectrometer. The morphology and microstructure of the samples were characterized by transmission electron microscopy (TEM, JEM-2100F) and scanning electron microscopy (SEM, SU 8230). Elemental distribution was analyzed using an energy-dispersive X-ray (EDX) spectrophotometer attached to the TEM. Nitrogen adsorption–desorption isotherms were measured using a BELSORP-Max analyzer. The chemical composition and elemental states were determined by X-ray photoelectron spectroscopy (XPS, Thermo Fisher ESCALAB Xi+). UV-Vis diffuse reflectance spectra were acquired using a PELambda950 spectrophotometer. Photoluminescence (PL) spectra were recorded on a PerkinElmer LS55 fluorophotometer. Electron paramagnetic resonance (EPR) signals were collected using an A300-9.5/12 spectrophotometer.

2.3.1 Photoelectrochemical measurements. A 300 W xenon lamp was used as the simulation sunlight source. The photocatalytic performance was evaluated using RhB as the target pollutant under visible light irradiation. 30 mg of the photocatalyst was dispersed in 30 mL of an aqueous RhB solution (0.1 g L^{-1}). The suspension was stirred in the dark for 0.5 h to achieve adsorption–desorption equilibrium, followed by irradiation under the xenon lamp. At 10-minute intervals, 1 mL of the solution was collected and filtered through a 0.22 μm membrane. The absorbance of the filtrate was measured using a UV-Vis spectrophotometer (Shimadzu UV3600) to determine the RhB concentration. The photocatalytic efficiency (η) was calculated using the following formula:[31]

$$\eta = C_t/C_0 \quad (1)$$

in which C_0 is the initial concentration of RhB (mg L^{-1}); C_t is the concentration of RhB after time t (mg L^{-1}). The reaction rate constant k_{obs} (min^{-1}) is calculated as:

$$\ln C_t = \ln C_0 - k_{obs} \times t \quad (2)$$

Electrochemical measurements were performed on a CHI electrochemical workstation (Shanghai Chenhua Instrument Co., Ltd, China) using a three-electrode system. Ag/AgCl and platinum were used as the reference and counter electrodes, respectively. The working electrode was prepared by depositing the catalyst on an FTO glass substrate with an active area of 2 × 2 cm^2. The electrolyte used was 0.5 M sodium sulfate. The electrode preparation process is detailed as follows: 5 mg of the photocatalyst was dispersed in 1 mL of ethanol containing 50 μL of Nafion (5 wt%, serving as a binder) *via* ultrasonic treatment for 30 min to form a homogeneous suspension. The FTO glass (2 × 2 cm^2) was pre-cleaned by sonication in ethanol and deionized water (15 min each) to remove surface contaminants. 100 μL of the suspension was drop-cast onto the FTO surface and dried at 60 °C for 2 h in air to form a uniform catalyst film. This procedure ensures good adhesion of the catalyst to the substrate and reproducible electrochemical performance.

2.3.2 Free radical trapping experiments. To identify the active species involved in the photocatalytic process, radical trapping experiments were conducted. Before illumination, 1 mL isopropanol (IPA), 0.1 g benzoquinone (BQ), and 0.3 g ethylenediaminetetraacetic acid (EDTA) were added to the RhB solution to scavenge hydroxyl radicals (·OH), superoxide radicals ($\cdot O_2^-$), and holes (h^+), respectively. The remaining procedures were identical to the photocatalytic degradation experiments. Accordingly, the photocatalytic reaction mechanism was further elucidated.

3 Results and discussion

3.1. Phase composition and FT-IR analysis

As illustrated in Fig. 1, the synthesis process involves three key steps. In step 1, bulk g-C_3N_4 (CN) is prepared through high-temperature polymerization, followed by exfoliation using pyrolysis and ultrasonic treatment. In step 2, Fe-MOF is synthesized *via* a hydrothermal method.[32] In step 3, Fe-MOF and CN are combined through calcination to form heterostructure MCN*x* heterojunction.

Fig. 2a shows the XRD patterns of CN and the MCN*x* heterojunction. For CN, the peaks at 12.9° and 27.5° correspond to the in-plane structural packing motif and the interlayer stacking of conjugated aromatic systems, respectively. Upon heterojunction formation, MCN*x* exhibits distinct peak shifts. Peaks at 12.9° and 27.5° correspond to the (100) in-plane structural packing and (002) interlayer stacking of g-C_3N_4 (PDF #87-1526), respectively. For Fe-MOF/g-C_3N_4 heterojunctions, new peaks at 24.1°, 33.1° and 35.6° are indexed to the (012), (104) and (110) planes of Fe-MOF (PDF #87-1165), confirming successful heterojunction formation without phase impurities.[32] In Fig. 2b and S1, the FT-IR spectra of Fe-MOF, CN and MCN*x* further validate the heterostructure. For Fe-MOF, the broad absorption peaks in the range of 3000–3500 cm^{-1} are attributed to the stretching vibrations of water molecules. Additionally, the characteristic peaks at 1590 cm^{-1} and 1388 cm^{-1} correspond to the asymmetric and symmetric stretching vibrations of O–C–O, respectively, confirming the presence of dicarboxylate ligands in Fe-MOF. The peak at 795 cm^{-1} is associated with the benzene ring vibrations.[33] For CN, the distinct peak at 812 cm^{-1} is assigned to the triazine unit, while the broad peaks in the range of 3000–3500 cm^{-1} arise from the stretching vibrations of N–H and O–H groups. The peaks between 1200 and 1700 cm^{-1} are attributed to the stretching vibrations of C–N heterocycles and C=N bonds.[34] The Fe-MOF FTIR spectrum in Fig. 2b is annotated with a peak at 550 cm^{-1}, attributed to the stretching vibration of Fe–O bonds in the MOF framework. In the MCN3-10 heterojunction, this peak is significantly weakened due to interfacial interactions: Fe^{3+} sites in Fe-MOF form coordinate bonds with N-containing groups (*e.g.*, $-NH_2$) in g-C_3N_4, reducing the electron density of Fe–O bonds and shifting their vibrational energy to lower intensities. This phenomenon confirms the formation of chemical bonds at the heterojunction interface. The FT-IR spectra demonstrate the formation of a heterostructure through the combination of Fe-MOF and CN.

3.1.1 Micromorphology characterizations. Fig. 3 and S2 present the SEM and TEM images of MCN*x* heterojunction. These images show that the interface contact area of MCN*x* heterojunction can be enlarged with the increase of Fe-MOF/CN ratio. However, excessive Fe-MOF loading (Fig. S2) causes particle aggregation and masks active sites. Among them, the Fe-MOF/CN heterojunction (MCN3-10) with the proper mass ratios of Fe-MOF to g-C_3N_4 (3 : 10) show relatively uniform Fe-MOF particles loaded on the thin porous CN layer. Therefore, the morphology, structure and electronic chemical state of MCN3-10 were mainly investigated. Fig. 3a displays the detailed microstructures of MCN3-10, bipyramidal Fe-MOF particles are embedded on the thin, porous layered CN (Fig. 3b). Lattice fringes with the spacings of 2.49 Å and 2.68 Å correspond to the (110) and (104) planes of Fe_2O_3, respectively (Fig. 3c), which is further verified by the selected-area electron diffraction (SAED) patterns (Fig. 3d). The EDS elemental mapping (Fig. 3e) demonstrates uniform distribution of C, N, O, and Fe, with the elongated bipyramidal Fe-MOFs embedded within the CN matrix. This optimized heterointerface facilitates efficient charge carrier separation and transport, thereby enhancing photocatalytic performance.

Nitrogen adsorption–desorption isotherms were employed to characterize the textural properties of the pristine CN, Fe-MOF and the MCN3-10 composite. As illustrated in Fig. 4a, all the samples exhibit Type IV isotherms with pronounced H3-type hysteresis loops, which are characteristic of mesoporous materials.[35] This confirms the presence of a well-defined mesoporous structure in all three materials. Fe-MOF displays a modest specific surface area of 38.535 m^2 g^{-1}, which is consistent with previously reported values for similar metal–organic frameworks.[36] In contrast, the flaky nanosheets of CN

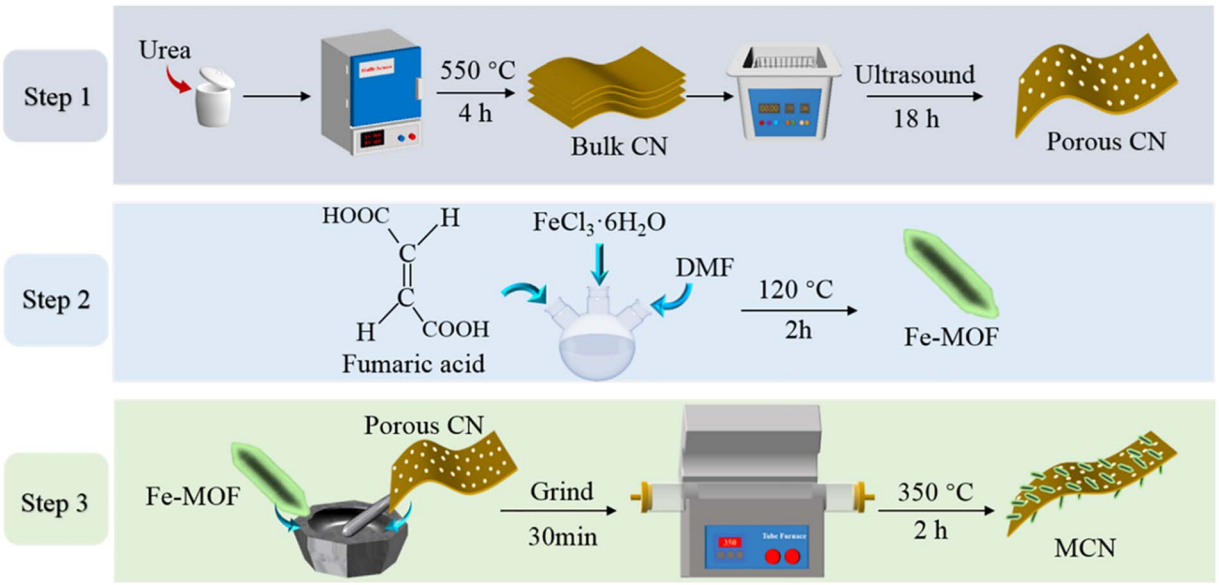

Fig. 1 Schematic of synthesis of Fe-MOF/CN.

yield a significantly higher surface area (96.283 $m^2 g^{-1}$), which can be attributed to its expanded interlayer spacing and accessible basal planes. Notably, the MCN3-10 heterostructure achieves the largest surface area (97.414 $m^2 g^{-1}$), indicating an optimized pore structure and enhanced material functionality. Complementary BJH pore size distributions (Table 1) further elucidate the hierarchical pore structure of these materials. The results indicate that MCN3-10 exhibits the most optimized pore volume and tailored mesoporosity, which provides abundant active sites and facilitates rapid mass transport of reactants and intermediates. This hierarchical pore structure is crucial for enhancing photocatalytic efficiency, as it allows for efficient diffusion of light, charge carriers, and reactants, thereby improving the overall reaction kinetics. Based on the nitrogen adsorption–desorption isotherms and BJH pore size distributions, the surface and pore characteristics of the CN, Fe-MOF and MCN3-10 composite were systematically analyzed. The MCN3-10 heterostructure, with its optimized pore structure and high surface area, is expected to exhibit superior photocatalytic performance compared to the other materials. These findings are supported by previous studies on g-C_3N_4-based composites,[20,37] where the formation of mesoporous structures has been shown to significantly enhance photocatalytic activity.

3.1.2 Compositions and chemical states. The chemical composition and interfacial bonding of the pristine CN, Fe-MOFs and MCN3-10 were characterized by XPS. Survey spectra (Fig. S3) confirm the presence of C, N, O and Fe in MCN3-10. The high-resolution C 1s spectrum is presented in Fig. 5a. For Fe-MOFs, the C 1s spectrum exhibits three peaks at binding energies of 284.8 eV (C–C), 286.2 eV (C–O–C) and 288.8 eV (O–C=O).[37] In contrast, the C 1s spectrum of CN is composed of two peaks at 284.8 eV (C–C) and 288.2 eV (N–C=N). For MCN3-10, the C–C peak remains at 284.8 eV, while the C–O peak shifts positively to 286.5 eV, as compared to Fe-MOFs. Additionally,

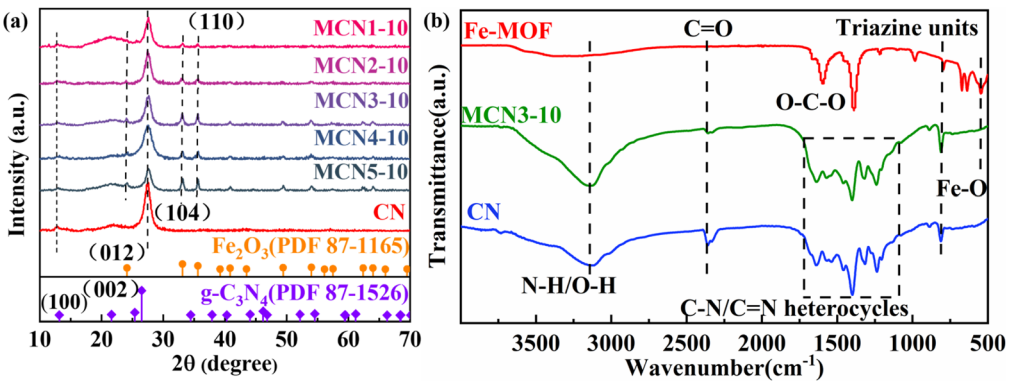

Fig. 2 (a) XRD patterns of CN and MCN*x* heterojunction, peaks at 12.9° and 27.5° correspond to (100) and (002) planes of g-C_3N_4 (PDF #87-1526), respectively. Peaks at 24.1°, 33.1° and 35.6° are indexed to the (012), (104) and (110) planes of Fe-MOF (PDF #87-1165), confirming successful heterojunction formation without phase impurities. (b) FT-IR spectra of Fe-MOF, MCN3-10, and CN.

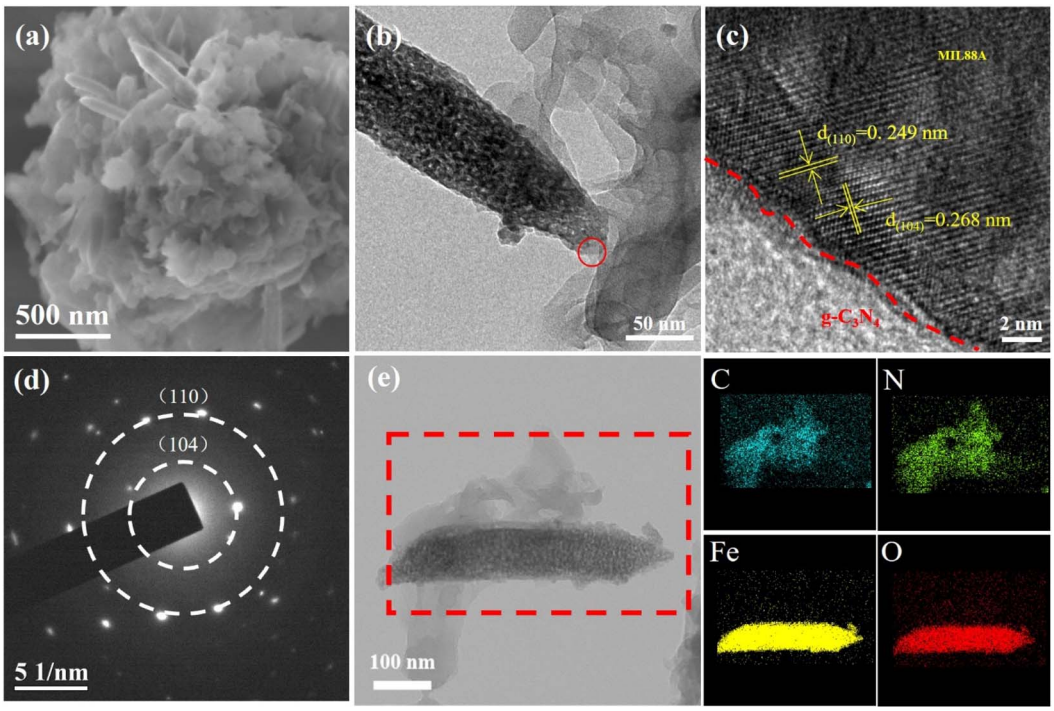

Fig. 3 (a) SEM and (b) TEM images of MCN3-10. (c) HR-TEM image of the heterojunction interface. (d) SAED pattern. (e) Elemental mapping of MCN3-10.

a unique peak shape at 288.2 eV is observed, attributed to the coexistence of C═O and N–C═N bonds. Fig. 5b displays the Fe 2p spectra of MCN3-10 and Fe-MOFs. In Fe-MOFs, five distinct peaks are observed at 712.0 eV (Fe^{2+} $2p_{3/2}$), 715.0 eV (Fe^{3+} $2p_{3/2}$), 718.7 eV (Fe^{3+} satellite peak), 725.8 eV (Fe^{2+} $2p_{1/2}$) and 730.7 eV (Fe^{3+} $2p_{1/2}$). For MCN3-10, the Fe 2p peaks shift negatively to 710.6 eV, 713.8 eV, 718.4 eV, 724.7 eV, and 730.5 eV, indicating strong interactions between Fe-MOF and CN. The O 1s spectrum of Fe-MOFs (Fig. 5c) reveals three peaks at 530.0 eV (H–O–H), 532.0 eV (Fe–O), and 533.9 eV (carboxyl groups). In MCN3-10, the H–O–H and Fe–O peaks shift positively to 530.1 eV and 532.1 eV, respectively. The N 1s spectrum of CN (Fig. 5d) is

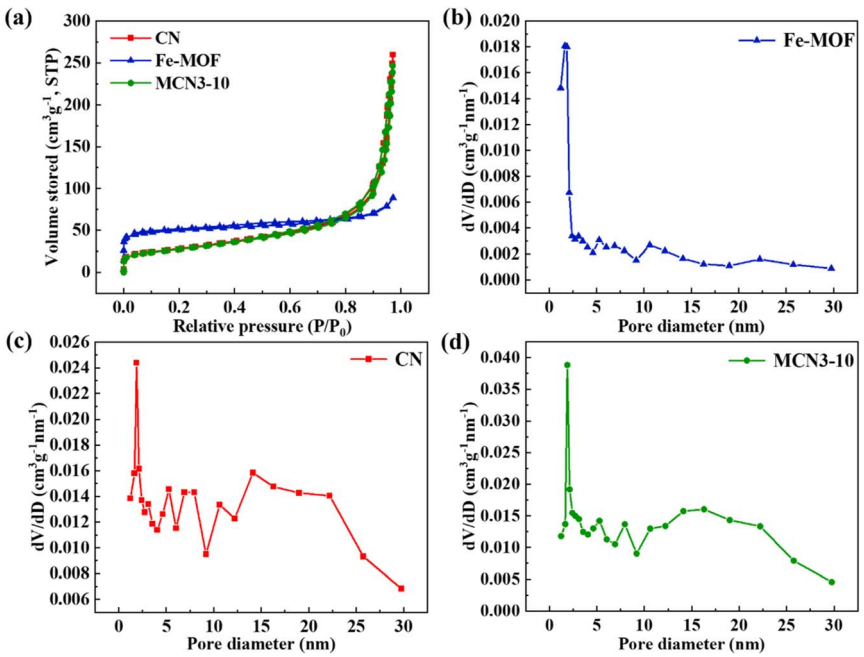

Fig. 4 (a) N_2 adsorption–desorption isotherms of CN, Fe-MOF, and MCN3-10. (b–d) Pore size distribution curves of CN, Fe-MOF, and MCN3-10.

Table 1 S_{BET}, pore volume caption, and pore diameter of CN, Fe-MOF and MCN3-10

Sample	S_{BET} ($m^2\ g^{-1}$)	Average pore size (nm)	Pore volume ($cm^3\ g^{-1}$)
CN	96.283	1.87	0.3807
Fe-MOF	38.535	1.65	0.6960
MCN3-10	97.414	1.87	0.3675

fitted into three main peaks at 398.6 eV (C–N=C), 400.6 eV (N–C_3) and 404.4 eV (π-excitation). For MCN3-10, these peaks shift slightly to 398.7 eV, 400.8 eV and 404.5 eV, respectively. It demonstrates electron transfer from CN to Fe-MOF, further supporting the formation of a heterostructure.[38]

3.1.3 Photocatalytic activity and stability. The photocatalytic activity of the samples was evaluated by degrading RhB in aqueous solution under a 300 W xenon lamp (RhB concentration: 100 mg L^{-1}; catalyst loading: 0.01 g). Fig. 6a shows the RhB degradation efficiency *versus* irradiation time. The MCN heterojunction exhibit significantly higher degradation rates than CN and Fe-MOF. The degradation rate of RhB is 99.56%, 91.20%, 81.57%, 79.02%, 73.19%, 70.57% and 11.53% for MCN3-10, MCN4-10, MCN2-10, MCN1-10, CN, MCN5-10 and Fe-MOF, respectively. Fig. 6b illustrates the time-dependent degradation profile for MCN3-10, the absorbance of RhB decreases with irradiation time and to zero after 40 min. The first-order rate constant (k_{obs}) of the degradation reaction is calculated by $\ln C_t = \ln C_0 - k_{obs}$,[39] C_t and C_0 are the concentrations of RhB at t and 0, respectively. Fig. 6c shows the results. MCN3-10 exhibits the highest first-order rate constant (k_{obs} =

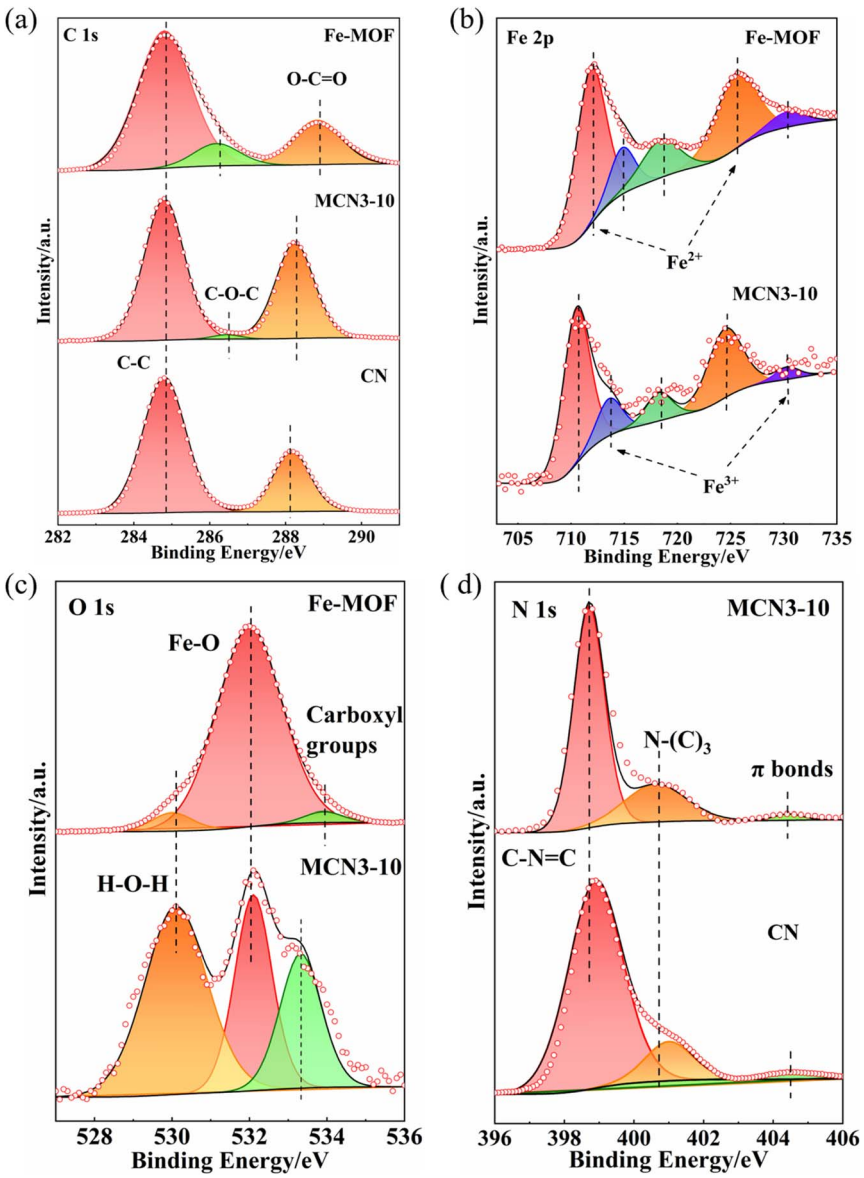

Fig. 5 XPS spectra of the pristine CN, Fe-MOFs and MCN3-10. (a) C 1s, (b) Fe 2p, (c) O 1s, (d) N 1s.

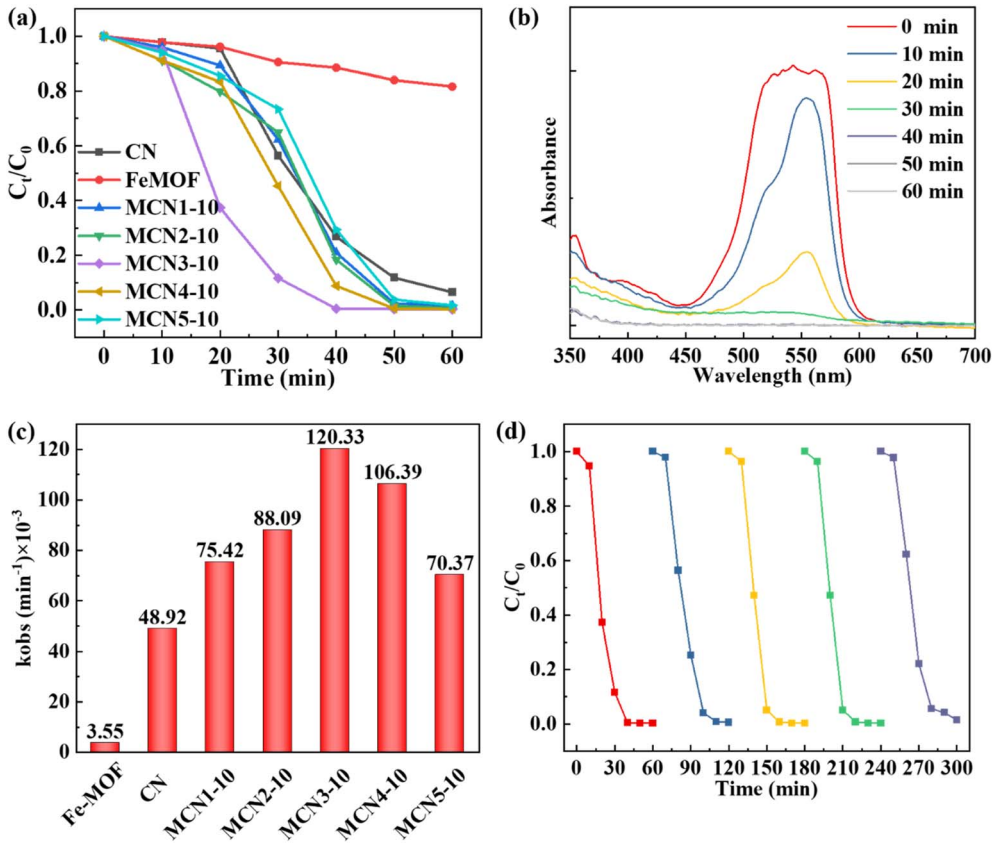

Fig. 6 (a) Photodegradation of RhB by different samples. (b) UV-vis spectra of RhB degraded by MCN3-10 under xenon lamp illumination. (c) Degradation rate constants of RhB for various samples. (d) Cycling experiments of photocatalytic RhB degradation using MCN3-10.

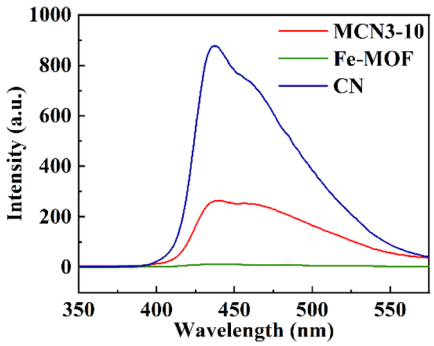

Fig. 7 The PL of CN, Fe-MOF, and MCN3-10.

120.33 × 10^{-3} min^{-1}), which is 33.9-fold and 2.5-fold higher than those of Fe-MOF (3.55 × 10^{-3} min^{-1}) and CN (48.92 × 10^{-3} min^{-1}), respectively. Cyclic degradation tests demonstrate the stability of MCN3-10 (Fig. 6d). After each cycle, the catalyst was washed and dried at 60 °C for 12 h. Remarkably, the degradation efficiency of RhB remains >90% after five consecutive cycles under 40 min illumination. The morphology of MCN3-10 (Fig. S5) remains consistent after cycling, with no obvious aggregation or dissolution of Fe-MOF particles. This structural stability aligns with the retention of Fe species within the composite. To directly observe the fitting quality and validate the kinetic model used for dye degradation. Fig. S4 shows the first-order kinetic plots of $\ln(C_t/C_0)$ *vs.* time for all samples (Fe-MOF, CN, MCN1-10, MCN2-10, MCN3-10, MCN4-10, and MCN5-10). These plots will clearly illustrate the linear fitting of degradation data to the first-order model, validating the calculated rate constants presented in Fig. 6c. The slope of each line corresponds to the rate constant (k), with MCN3-10 showing the steepest slope, visually confirming its fastest degradation rate.

3.1.4 Photoelectrochemical analysis. Fig. 7 shows the photoluminescence (PL) spectra of the MCN3-10 composite under excitation at 360 nm. The Fe-MOF exhibits negligible luminescence, which is attributed to its inherent rapid non-radiative recombination of photo-generated charge carriers. In contrast, the pristine CN displays a prominent emission peak at 437 nm, corresponding to the recombination of electron–hole pairs across the bandgap. Notably, the MCN3-10 composite exhibits a redshifted emission peak at 441 nm, accompanied by a significant reduction in luminescence intensity (over 70% compared to the pristine CN). This observation strongly suggests an efficient interfacial charge transfer mechanism, likely operating *via* the S-scheme charge transfer mechanism,[40] which effectively suppresses the recombination of electron–hole pairs. In the MCN3-10 heterostructure, photogenerated electrons in the conduction band of CN are preferentially transferred to the valence band of Fe-MOF, thereby promoting

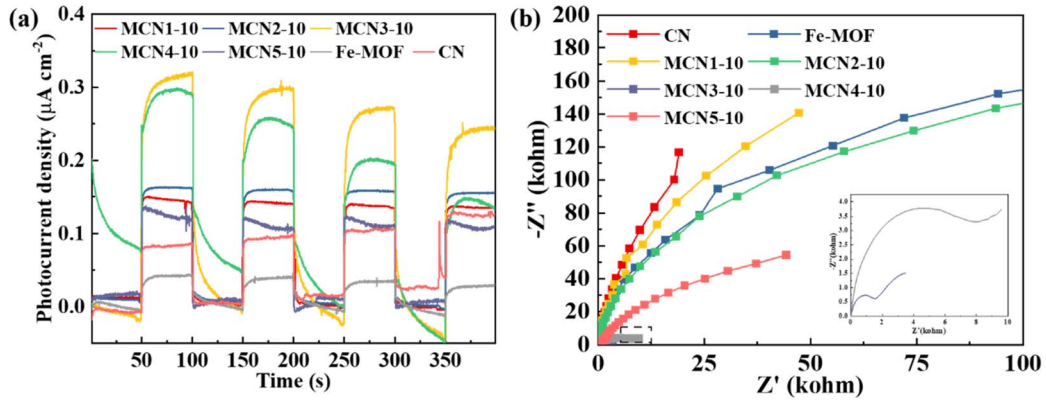

Fig. 8 The TPR (a) and EIS (b) of all the photocatalysts.

directional carrier migration and reducing the probability of recombination. This enhanced charge separation mechanism contributes to the extended lifetime of photogenerated carriers and facilitates the efficient generation of reactive oxygen species (ROS), which are critical for pollutant degradation. Consequently, the MCN3-10 composite demonstrates superior photocatalytic performance compared to the individual components, highlighting the importance of heterojunction formation in enhancing the overall reaction kinetics.

Transient photocurrent response (TPR) was measured to further probe charge carrier separation efficiency.[41] As shown in Fig. 8a, CN and Fe-MOF exhibit low photocurrent intensities and thus inefficient charge separation. In contrast, MCN*x* heterojunction demonstrate significantly enhanced

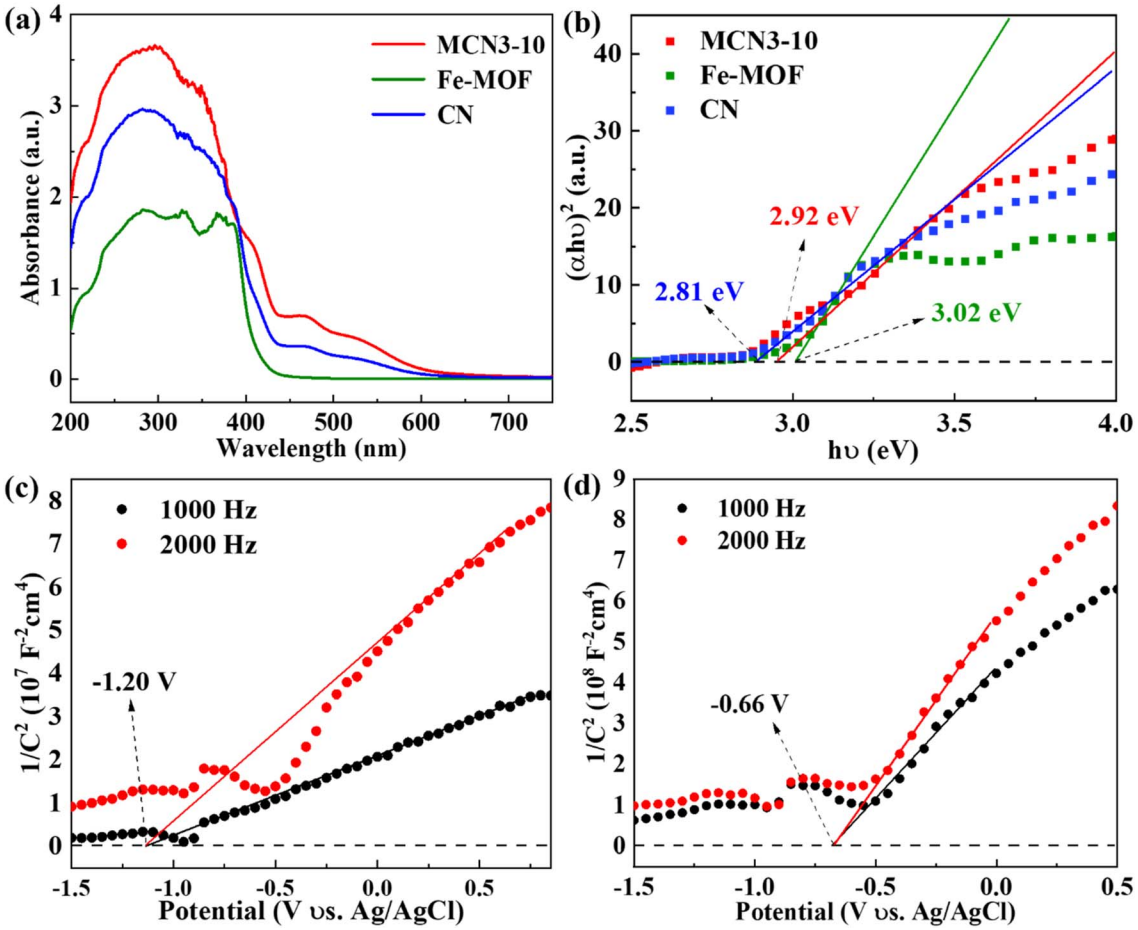

Fig. 9 (a) UV-vis diffuse reflectance spectra and (b) Tauc plots of CN, Fe-MOF, and MCN3-10. Mott–Schottky plots of (c) Fe-MOF and (d) CN in 0.5 mol per L Na_2SO_4 aqueous solution (pH 7.0).

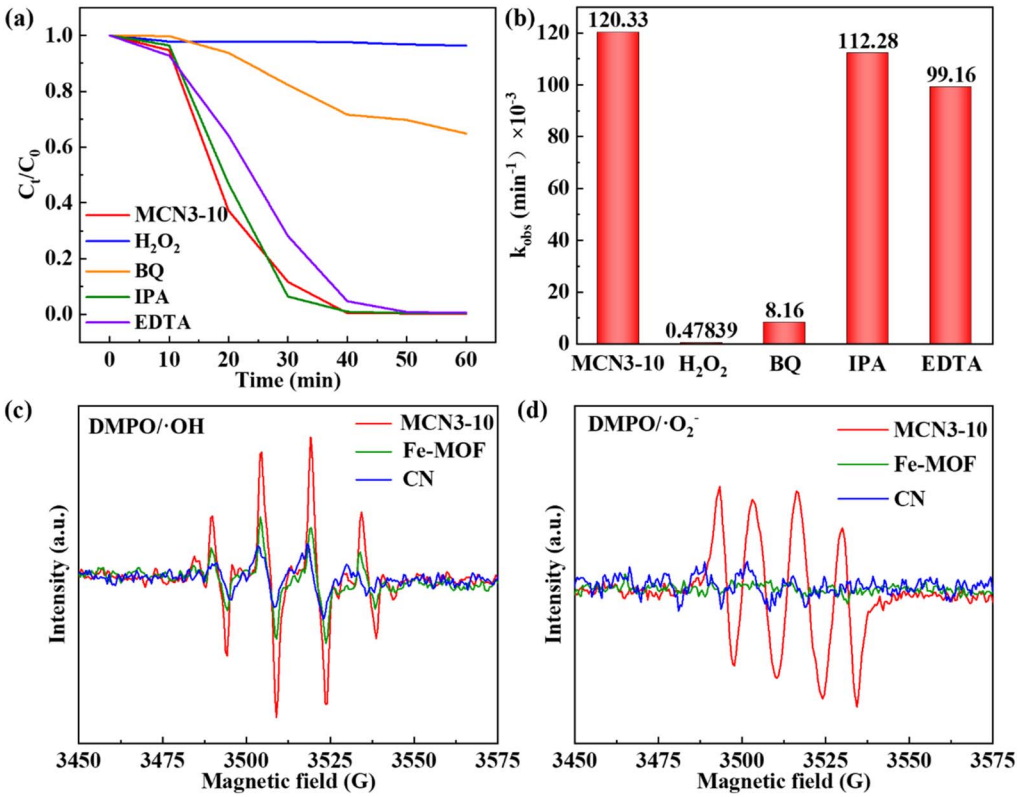

Fig. 10 (a) Free radical trapping experiments for the degradation of RhB by MCN3-10. (b) Degradation rate constants of RhB in free radical trapping experiments over 40 minutes. EPR spectra of (c) DMPO/·OH and (d) DMPO/·O_2^-.

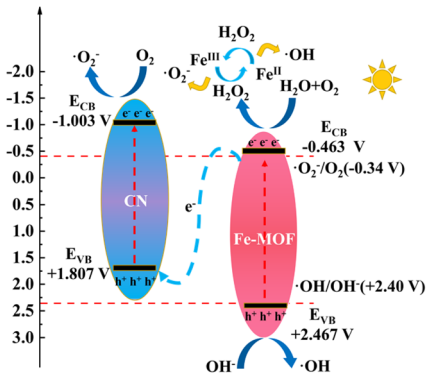

Fig. 11 Photocatalytic mechanism for the degradation of RhB on MCN3-10.

performances with the photocurrent intensity in the order: MCN3-10 > MCN4-10 > MCN2-10 > MCN1-10 > MCN5-10 > CN > Fe-MOF. Notably, MCN3-10 achieves the highest photocurrent intensity, reflecting superior charge separation capability. Fig. 8b shows the electrochemical impedance spectroscopy (EIS). MCN3-10 exhibits the lowest charge transfer resistance at the electrolyte–catalyst interface, which further demonstrates the exceptional charge carrier separation and transport properties, accounting for its enhanced photocatalytic activity.

3.1.5 Photocatalytic mechanism. The enhanced photocatalytic performance of MCN3-10 was further elucidated through UV-vis diffuse reflectance spectroscopy (DRS) and band structure analysis. As shown in Fig. 9a, Fe-MOF exhibits a distinct absorption edge at 440 nm within the ultraviolet region, while pristine g-C_3N_4 (CN) demonstrates broad absorption spanning both UV and visible spectra. Significantly, the MCN3-10 composite manifests markedly enhanced light harvesting across this spectral range. Fig. 9b displays the Tauc plots from the Kubelka–Munk equation $(\alpha h\nu)^n = A\ (h\nu - E_g)$,[42] yielding the bandgap energies of 2.81 eV (CN), 3.02 eV (Fe-MOF), and 2.92 eV (MCN3-10). Mott–Schottky (M–S) analysis was employed to determine band positions. On the M–S curve, the flat band voltages of CN and Fe-MOF are −1.20 and −0.66 V *vs.* Ag/AgCl, respectively (Fig. 9c and d). Based on $E_{NHE} = E_{Ag/AgCl} + 0.197$, the calculated results of CN and Fe-MOF are −1.00 V and −0.463 V *vs.* NHE. For n-type semiconductors, the conduction band (CB) potential approximates the flat-band potential. Thus, the CB positions of CN and Fe-MOF are estimated to be −1.00 V and −0.463 V *vs.* NHE, respectively. Valence band (VB) positions were calculated using $E_{VB} = E_g + E_{CB}$.[43] The VB positions of CN and Fe-MOF are calculated to be 1.807 V and 2.557 V *vs.* NHE, respectively. This staggered band alignment establishes a thermodynamic driving force for S-scheme charge transfer: the photogenerated electrons in the CB of Fe-MOF (−0.463 V) recombine with the holes in the VB of CN (1.807 V); residual electrons are accumulated in the CB of CN (−1.00 V) for $O_2 \rightarrow \cdot O_2^-$ reduction (requiring −0.33 V); holes in the VB of Fe-MOF (2.557 V) drive $H_2O \rightarrow \cdot OH$ oxidation (requiring 2.38 V). The

optimized energy landscape minimizes recombination losses while maximizing redox potential in the MCN3-10 heterojunction, thereby amplifying photocatalytic degradation efficiency.

Free radical trapping experiments were conducted to identify active species in the photocatalytic degradation of RhB by MCN3-10. Isopropanol (IPA), benzoquinone (BQ), and ethylenediaminetetraacetic acid (EDTA) served as scavengers for hydroxyl radicals ($\cdot OH$), superoxide radicals ($\cdot O_2^-$), and holes (h^+), respectively.[44,45] As shown in Fig. 10a and b, the addition of BQ significantly reduces the degradation rate of RhB, confirming $\cdot O_2^-$ as the dominant active species. The degradation rate is also slowed by the addition of EDTA, suggesting that h^+ contributes to the photocatalytic reaction. In contrast, IPA and H_2O_2 show negligible effects on the degradation of RhB. Electron paramagnetic resonance (EPR) spectroscopy was employed to further confirm the active species generated during photocatalysis. As shown in Fig. 10c, distinct $\cdot OH$ signals appeared only in illuminated MCN3-10, absent in Fe-MOF or CN. This is attributed to the S-scheme charge transfer mechanism, as the redox potentials of $\cdot OH/H_2O$ (+1.99 V *vs.* NHE) and $\cdot OH/OH^-$ (+2.40 V *vs.* NHE) achievable through S-scheme-mediated charge separation. Fig. 10d reveals strong $\cdot O_2^-$ signals in MCN3-10 under illumination, generated *via* the Fe^{2+}/Fe^{3+} redox cycle in the photo-Fenton process. In brief, $\cdot O_2^-$ and h^+ serve as primary active species, with $\cdot OH$ playing a secondary role through S-scheme-enhanced charge transfer.

Fig. 11 schematically illustrates the photocatalytic mechanism of MCN3-10. Under solar irradiation, electrons transition from the VB to the CB in both CN and Fe-MOF. The S-scheme heterojunction inhibits recombination of electrons in the CB of Fe-MOF with holes in the VB of CN, resulting in electron accumulation in the CB of CN and hole accumulation in the VB of Fe-MOF. This charge separation promotes generation of ROS, including $\cdot OH$ and $\cdot O_2^-$. Concurrently, photo-Fenton reactions occur on MCN3-10: electrons from Fe-MOF react with O_2 adsorbed on the porous surface to produce H_2O_2, which subsequently reacts with Fe^{2+} and Fe^{3+} sites in Fe-MOF to generate additional $\cdot OH$ and $\cdot O_2^-$ through the photo-Fenton process. These reactive species, combined with photogenerated holes (h^+), effectively degrade RhB dye into small organic fragments, CO_2, and H_2O. This synergistic mechanism underpins the high-efficiency photocatalytic degradation of RhB. Table S1 has summarized recent studies on MOF/g-C_3N_4-based photocatalysts for RhB degradation. The table includes key parameters: synthesis method, catalyst dosage, light source (power/wavelength), degradation time, first-order rate constant (k), and stability (cycles). MCN3-10 heterojunction exhibits a superior k value (120.33×10^{-3} min^{-1}) and shorter degradation time (40 min) compared to most reported systems (*e.g.*, MOF-5/g-C_3N_4, 90 min; Fe_2O_3/g-C_3N_4, 150 min). Additionally, the electrostatic self-assembly synthesis in this word is simpler than hydrothermal or solvothermal methods in referenced works, highlighting the practical advantage of our approach. Furthermore, compared with the recent research results,[46–48] the Fe-MOF/g-C_3N_4 heterojunction in this word balances high catalytic activity with sustainable synthesis: low-cost precursors, simplified procedures, minimal solvent usage, and long-term reusability. These features, combined with its superior degradation efficiency over adsorption or single-component catalysts, highlight its potential for scalable environmental remediation.

4 Conclusions

Porous Fe-MOF/CN (MCNx) heterojunction were successfully synthesized *via* a facile calcination method. Under simulated sunlight irradiation, the optimized MCN3-10 heterojunction demonstrate exceptional photocatalytic activity for RhB degradation. The results reveal a 33.9-fold enhancement in photocatalytic performance compared to pristine Fe-MOF and a 2.5-fold improvement *versus* CN. Recycling experiments confirm exceptional stability and reusability of MCN3-10 for RhB degradation. Electrochemical characterization and photoluminescence (PL) spectroscopy indicate that interfacial electron transfer between CN and Fe-MOF is pivotal for enhancing photocatalytic performance. Radical trapping experiments further demonstrate that RhB degradation by MCN3-10 is predominantly mediated by superoxide radicals ($\cdot O_2^-$). This study provides novel mechanistic insights into photocatalytic degradation processes and establishes MCN3-10 as a high-performance, stable photocatalyst for environmental remediation applications.

Author contributions

Hongqiang Xin: conceptualization, methodology, investigation, data analysis, writing – original draft, and writing – review and editing. Fei Ma: supervision, validation, and funding acquisition. Jingpu Zhang, Zeming Lin and Wei Li: investigation and data analysis.

Conflicts of interest

There are no conflicts to declare.

Data availability

The data that support the findings of this work are available from the corresponding author [H. Xin] upon reasonable request.

SI associated with this article can be found in the online version. See DOI: **https://doi.org/10.1039/d5ra04928h**.

Acknowledgements

This work was jointly supported by the National Natural Science Foundation of China (22001202), the Innovation Foundation of Gansu Provincial Department of Education (2025B-058), The Joint Foundation of Southwest Jiaotong University and Lanzhou Jiaotong University (1200150725).

Notes and references

1 M. Salehi, *Environ. Int.*, 2022, **158**, 106936.

2 W. Musie and G. Gonfa, *Heliyon*, 2023, **9**, e18685.
3 J. Huo and C. Peng, *Resour. Policy*, 2023, **86**, 104049.
4 M. Ahmed, M. O. Mavukkandy, A. Giwa, M. Elektorowicz, E. Katsou, O. Khelifi, V. Naddeo and S. W. Hasan, *npj Clean Water*, 2022, **5**, 1–25.
5 G. I. Edo, L. O. Itoje-akpokiniovo, P. Obasohan, V. O. Ikpekoro, P. O. Samuel, A. N. Jikah, L. C. Nosu, H. A. Ekokotu, U. Ugbune, E. E. A. Oghroro, O. L. Emakpor, I. E. Ainyanbhor, W. A.-S. Mohammed, P. O. Akpoghelie, J. O. Owheruo and J. J. Agbo, *Ecol. Front.*, 2024, **44**, 874–889.
6 M. Mumba, H. Ovink and J. Rockström, *Nat. Water*, 2025, **3**, 356–357.
7 P. K. Singh, U. Kumar, I. Kumar, A. Dwivedi, P. Singh, S. Mishra, C. S. Seth and R. K. Sharma, *Environ. Sci. Pollut. Res.*, 2024, **31**, 56428–56462.
8 V. Saxena, *Water Air Soil Pollut.*, 2025, **236**, 73.
9 R. Fatmawati, I. Dewata, E. Nasra and R. D. Y. Away, *Jurnal Pijar MIPA*, 2025, **20**, 325–333.
10 Y. Pan, R. Abazari, B. Tahir, S. Sanati, Y. Zheng, M. Tahir and J. Gao, *Coord. Chem. Rev.*, 2024, **499**, 215538.
11 S. Yang, S. Sun, Z. Xie, Y. Dong, P. Zhou, J. Zhang, Z. Xiong, C.-S. He, Y. Mu and B. Lai, *Environ. Sci. Technol.*, 2024, **58**, 19571–19583.
12 J. Xiao, S. Guo, D. Wang and Q. An, *Chem.–Eur. J*, 2024, **30**, e202304337.
13 X. Tao, X. Yuan, L. Huang, S. Shang and D. Xu, *RSC Adv.*, 2020, **10**, 36363–36370.
14 J. Joseph, S. Iftekhar, V. Srivastava, Z. Fallah, E. N. Zare and M. Sillanpää, *Chemosphere*, 2021, **284**, 131171.
15 A. K. Juma, Z. M. A. Merican and A. Haruna, *Chem. Eng. Res. Des.*, 2024, **208**, 391–435.
16 L. He, Y. Zhang, Y. Zheng, S. Shan and Y. Dong, *J. Porous Mater.*, 2019, **26**, 1839–1850.
17 H. Zhang, X. Gong, Z. Song, S. Zhang, W. Du, T. T. Nguyen, M. Guo and X. Gao, *Opt. Mater.*, 2021, **113**, 110865.
18 N. Hussain, H. Alawadhi and M. Ali Abdelkareem, *Crit. Rev. Solid State Mater.*, 2025, 1–31, DOI: **10.1080/10408436.2025.2507894**.
19 T. Bao, X. Li, S. Li, H. Rao, X. Men, P. She and J. Qin, *Nano Mater. Sci.*, 2025, **7**, 145–168.
20 T. Muhmood, I. Ahmad, Z. Haider, S. K. Haider, N. Shahzadi, A. Aftab, S. Ahmed and F. Ahmad, *Mater. Today Sustainability*, 2024, **25**, 100633.
21 W. Mišta, G. Dovbeshko, M. Chaika, P. Wiewiórski, M. Ptak, V. Boiko and W. Stręk, *Low Temp. Phys.*, 2023, **49**, 296.
22 S. S. A. Shuaib, Y. Lu, Q. Wang, Y. Chen, M. Cai, Y. Wei and S. Sun, *ChemCatChem*, 2025, **17**, e202402152.
23 P. Bharathi, N. Chidhambaram and A. Thirumurugan, *J. Mater. Res.*, 2023, **38**, 4736–4746.
24 J. Yamini, R. Dhanabal, P. Gomathi Priya and M. Induja, *Mater. Chem. Phys.*, 2025, **333**, 130323.
25 W. Liu, J. Zhang, Q. Kang, H. Chen and R. Feng, *Ecotoxicol. Environ. Saf.*, 2023, **252**, 114611.
26 Z. Jia, F. Lyu, L. C. Zhang, S. Zeng, S. X. Liang, Y. Y. Li and J. Lu, *Sci. Rep.*, 2019, **9**, 7636.
27 Q. Huang, X. Guo, Y. Fu, L. Yang and J. Meng, *Mater. Lett.*, 2024, **364**, 136119.
28 H. Zhang, Y.-H. Luo, F.-Y. Chen, W.-Y. Geng, X.-X. Lu and D.-E. Zhang, *J. Hazard. Mater.*, 2023, **441**, 129875.
29 M. H. Dang Thi, L. G. Hoang Thi, C. D. Huynh, H. P. Nguyen Thi and D. D. La, *RSC Adv.*, 2024, **14**, 20543–20552.
30 X.-F. Zhang, T.-L. Chang, N. Guo, G.-L. Jia, X.-B. Li, Z.-Y. Zhao, H. Wang, J.-C. Wang, X.-F. Wu, C.-S. Pan, L. Liu and L.-L. Yang, *J. Inorg. Organomet. Polym. Mater.*, 2024, **34**, 1309–1324.
31 Z. He, L.-L. Tong, Z.-P. Zhang, J.-M. Chen and S. Song, *Acta Phys.-Chim. Sin.*, 2015, **31**, 2341–2348.
32 Y. Pan, X. Hu, D. Shen, Z. Li, R. Chen, Y. Li, J. Lu and M. Bao, *Sep. Purif. Technol.*, 2022, **295**, 121216.
33 X. Jia, J. Zhang, J. Qiao, Z. Song, X. Xu, L. Zhang, X. Wang, G. Zhu and S. Jiao, *J. Catal.*, 2025, **450**, 116297.
34 U. Sahoo, S. Pattnayak, S. Choudhury, P. Aparajita, S. Das and G. Hota, *Opt. Mater.*, 2025, **160**, 116778.
35 X. Song, X. Zhou and X. Lv, *Asian Earth Sci.*, 2023, **247**, 105595.
36 X. Wang, D. Xu, D. Yu, J. Liang, X. Liang and Q. Shou, *J. Environ. Chem. Eng.*, 2024, **12**, 111600.
37 A. Rodríguez-Gómez, S. Ould-Chikh, J. Castells-Gil, A. Aguilar Tapia, P. Bordet, M. Alrushaid, C. Martí-Gastaldo and J. Gascon, *ACS Catal.*, 2022, **12**, 3832–3844.
38 B. Zhang, L. Zhang, K. Akiyama, P. A. Bingham, Y. Zhou and S. Kubuki, *ACS Appl. Mater. Interfaces*, 2021, **13**, 22694–22707.
39 M. Zhang, Y. Wang, J. Liu, M. Thangamuthu, Y. Yue, Z. Yan, J. Feng, D. Zhang, H. Zhang, S. Guan, M.-M. Titirici, I. Abrahams, J. Tang, Z. Zhang, S. Dunn and H. Yan, *J. Mater. Chem. A*, 2021, **9**, 22861–22870.
40 L. Zhang, J. Zhang, H. Yu and J. Yu, *Adv. Mater.*, 2022, **34**, e2107668.
41 H. He, R. Shen, Y. Yan, D. Chen, Z. Liu, L. Hao, X. Zhang, P. Zhang and X. Li, *Chem. Sci.*, 2024, **15**, 20002–20012.
42 J. Tauc, R. Grigorovici and A. Vancu, *Phys. Status Solidi B*, 1966, **15**, 627–637.
43 A. Anjum Moinuddin, A. Vijay Kotkondawar, G. Hippargi, A. Anshul and S. Rayalu, *Appl. Surf. Sci.*, 2022, **597**, 153554.
44 C. Zhou, Z. Liu, L. Fang, Y. Guo, Y. Feng and M. Yang, *Catalysts*, 2020, **10**, 317.
45 P. Debes, M. Pagel, S. Muntean, J. Hessling, B. Smarsly, M. Schönhoff and T. Gatti, *Photochem*, 2024, **5**, 1.
46 E. Salama, M. Ghanim, H. S. Hassan, W. A. Amer, E.-Z. M. Ebeid, A. H. El-Shazly, M. Ossman and M. F. Elkady, *RSC Adv.*, 2022, **12**, 18363–18372.
47 S. Sarkar and C. Upadhyay, *Catal. Today*, 2025, **445**, 115101.
48 L. Shupletsov, A. C. Schieck, I. Senkovska, V. Bon and S. Kaskel, *Green Chem.*, 2025, DOI: **10.1039/D5GC01029B**.